Void growth measurement and modelling in a thermosetting epoxy resin using SEM and tomography techniques

Jan Rojek, Christian Breite, Yentl Swolfs, Lucien Laiarinandrasana

Continuum Mechanics and Thermodynamics manuscript No.
(will be inserted by the editor)

Void growth measurement and modelling in a thermosetting epoxy resin using SEM and tomography techniques

Jan Rojek · Christian Breite · Yentl Swolfs · Lucien Laiarinandrasana

Received: date / Accepted: date

Abstract Void growth and failure in an epoxy resin is investigated. Tensile tests are carried out on double-notched round bars. Stress triaxiality in the net section is controlled by the use of two different notch root radii. SEM and computed tomography observations are conducted on regions of interest to identify voids and evaluate their growth. Failure initiation sites are analyzed, revealing critical defects in the form of voids or particles. The macroscopic and microscopic experimental results are used to optimize the Gurson-Tvergaard-Needleman model. A finite element analysis is performed to study the mechanical response of the notched specimens. The peaks of the maximum principal stress are found to coincide with the locations of the failure initiation sites observed experimentally and the model is shown to be able to handle non-uniform initial void distributions.

Keywords Epoxy · Failure criterion · Constitutive modelling · Elasto-viscoplasticity · Finite element method

1 Introduction

Thermosetting epoxy resins are widely used as matrix materials in fibre-reinforced composites. They offer good mechanical properties, as well as chemical, electrical and elevated temperature resistance. Due to their numerous advantages, epoxy resins have become the most common choice in high-performance

J. Rojek, L. Laiarinandrasana
MINES ParisTech, PSL University
Centre des Matériaux (CMAT), CNRS UMR 7633
BP 87 91003 Evry Cedex, FRANCE
Tel.: +33 01 60 76 30 42
E-mail: jan.rojek@mines-paristech.fr

C. Breite, Y. Swolfs
Department of Materials Engineering, KU Leuven
Kasteelpark Arenberg 44 bus 2450, 3001 Leuven, BELGIUM

composite applications, e.g. in airframes. Epoxy, as other thermosets, fails in a brittle fashion at low strains due to strong cross-linking.

To study the micromechanical behaviour of composites, it is necessary to characterize the mechanical properties of the resin. Tensile strength of polymers is routinely measured under uniaxial conditions. However, it is not clear how well these measured properties represent resin behaviour inside a composite. Locally, the polymeric matrix can experience significant deformations under multiaxial stresses [1]. This is true both for matrix-driven failure modes, as well as for fibre-dominated failure. In the latter case, single filament breaks cause local overstressing, which can lead to a formation of fibre break clusters [2]. The redistribution of stress onto the neighbouring fibres depends strongly on the properties of the matrix, which is subjected to a multiaxial and dynamic stress state [3]. It is therefore desirable to characterize the mechanical response of the polymer taking into account more complex loading conditions.

Another aspect to consider is the presence of voids in the resin. They are commonly encountered at different scales of the composite. Void growth and the influence of stress triaxiality have been studied in several thermoplastic semi-crystalline polymers, e.g. by Laiarinandrasana et al. [4], Challier et al. [5], Boisot et al. [6], Selles et al. [7]. In turn, thermosetting polymers, such as epoxy, have been usually considered to fail in a brittle fashion, without observable void growth [8].

The objective of the study described here is to quantify void growth inside a thermosetting epoxy resin and provide an interpretation of the damage evolution. To this end, double-notched round bars were tested in tension. The triaxiality ratio was controlled by modifying the notch root radius. SEM and computed tomography techniques were used to evaluate in detail void growth inside the material. The next step consisted in optimizing a Gurson-Tvergaard-Needleman (GTN) material behaviour [9] to model the void growth and stress state in the tested specimens. The aforementioned studies on thermoplastics used the GTN model under the assumption of a homogeneous initial porosity distribution [10][11]. A critical void fraction criterion was used [5][6], while in epoxy failure is typically linked to the presence of a critical defect [12]. In the study presented, a brittle failure criterion is proposed and a non-uniform initial void distribution is taken into account. The obtained experimental and numerical results offer an insight into the mechanics of a thermosetting epoxy, improving the understanding of its failure and the damage processes that lead to it.

2 Material and methods

2.1 Epoxy resin material and specimen geometries

"In-house prepregging" epoxy Sicomin SR 8500 / KTA 313 slabs were produced, using a method similar to that described by Morelle et al. [8]. The manufacturing process consisted of several steps. At first, the bisphenol-A

type epoxy resin and the diamine hardener were degassed individually for 60 min at 70 °C. In a second step, the two components were thoroughly mixed and degassed again for 10 min at 70 °C. The degassed mixture was then poured into cylindrical glass moulds, coated with a high slip mould release agent Chemlease PMR-90 EZ. The filled moulds were held for 60 min at 70 °C in a convection oven, before the temperature was ramped up from 70 °C to 120 °C over a period of 50 min. The temperature was then held constant for 90 min. Once the curing step was finished, the oven was cooled down over a period of 120 min.

Axisymmetric double-notched round bars were machined from the obtained cylindrical epoxy slabs. The geometry of the specimens is shown in Figure 1. Two notch root radii were studied: 6 mm and 1 mm. The specimens are identified as NTx-y, where NT stands for "notched tensile", x is the notch root radius in millimetres and y is the specimen number. For both specimen geometries, the diameter outside the notch (gauge diameter) is 7 mm and notch depth is 1 mm, resulting in the net section diameter of 5 mm and a notch-to-depth ratio of 0.29.

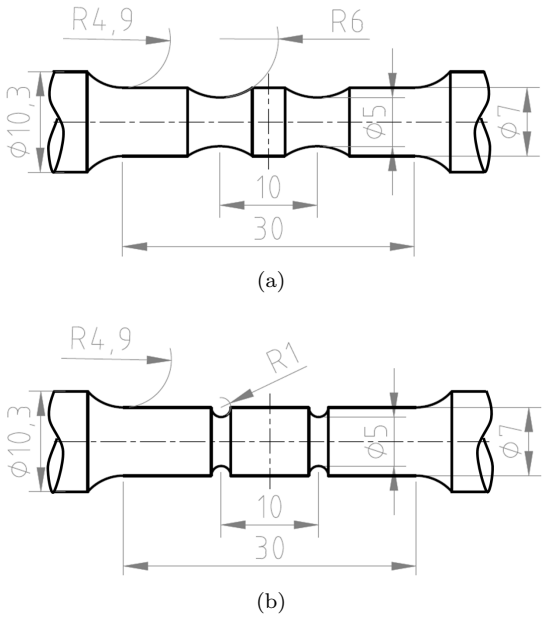

Fig. 1 Specimen geometry: **a)** NT6 and **b)** NT1. All dimensions are in mm.

Single and double-notched specimens similar to the ones described above have been used in a number of previous studies on damage development and failure in semi-crystalline polymers [4][6][7][10][11]. In smooth (unnotched) specimens under a tensile load, a multiaxial stress state develops locally with the onset of necking. However, the location of the necked region cannot be

controlled. Introducing a notch localizes the multiaxial stress region and mimics a necked specimen. This is particularly helpful in case of a brittle material, like the epoxy studied here, which otherwise exhibits little observable necking.

In the study presented, it was desirable to stop mechanical tests shortly prior to failure and observe damage development. However, the moment of interrupting the test is hard to determine for a brittle material. That problem was solved by using a double-notched geometry. When under load, both notches experience the same stress state. Eventually, a critical defect causes one of them to fail, while the other one is abruptly unloaded.

2.2 Tensile tests

The double-notched specimens described above were loaded in tension until failure on an electromechanical tensile rig with displacement control. All tests were carried out at room temperature. The cross head speed was 0.2 mm/s and 2.0 mm/s for NT1 and 0.2 mm/s for NT6 specimens. The initial grip distance was 39.6 mm for all tests. At least two specimens were tested for each combination of geometry and loading rate.

The testing rig was equipped with a video acquisition setup. Photographs were recorded during the tests at a rate of at least two frames per second. From the obtained images, approximately fifteen were selected for each specimen, in order to capture the characteristic moments of the entire test. From these photographs, several local displacements were measured using an open-source image analysis software Fiji [13], in locations shown in Figure 2. The following measurements were taken:

- axial displacement between point markers on the external sides of the notches ($\Delta L = L - L_0$)
- notch opening displacement ($NOD = (a - a_0)/2$)
- radial reduction ($\Delta R = R_0 - R$)

Notch opening displacement was calculated as a mean of four measurements (on both sides of the two notches). Similarly, radial reduction values were averaged over both notches. The local character of these measurements is particularly important in case of notched specimens, where cross head displacement provides purely macroscopic information on the deformation process.

2.3 Scanning Electron Microscopy - Fractography

Scanning Electron Microscopy was used to observe the fracture surfaces of the broken notches of four specimens: NT6-1, NT6-2, NT1-1 and NT1-2. The observations were carried out on a FEI Nova NanoSEM 450, at 5 kV voltage and 50 pA current. A 9 nm Au/Pd coating was applied to improve conductivity. The objective was to study the morphology of the fracture surfaces and the location of the fracture initiation sites. Furthermore, the images were used to extract information about microscopic voids: their location, number and size.

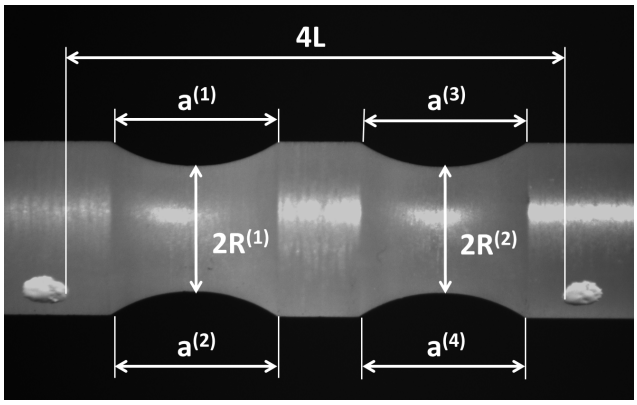

Fig. 2 Macroscopic measurements.

Approximately 25 % of each specimen's fracture surface was mapped at a 250× magnification. This ensured sufficient resolution to identify the voids. Up to fifty individual scans were digitally merged for each specimen using the Fiji stitching tool [14]. Voids were then counted manually and their spatial coordinates and maximum Feret diameters [15] were measured. Then, each void's cross-sectional area was estimated as that of a circle with its diameter equal to the void's maximum Feret diameter.

2.4 Synchrotron Radiation Computed Tomography

After tensile testing, voids in the unbroken notches of the aforementioned four specimens (NT6-1, NT6-2, NT1-1 and NT1-2) were observed using Synchrotron Radiation Computed Tomography (SRCT). SRCT offers a much higher radiation intensity than laboratory micro-computed tomography, allowing fast imaging at sub-micron resolutions. It is a convenient non-destructive method of imaging microstructures in three dimensions. The scans were obtained on the ANATOMIX beamline of Synchrotron SOLEIL (France) [16]. Radiographs were taken at 2000 angular positions during a 180° rotation lasting approximately 7 min, with a 16 keV beam energy. The voxel size was 650 nm.

Each scan covered a cylinder with both height and diameter equal to 1.3 mm, resulting in a volume of 1.73 mm^3. These volumes will from now on be referred to as Tomographic Volumes of Interest (TVOI). It would have been very time-consuming to image the entire specimens at a resolution allowing void characterization. Therefore, it was necessary to choose characteristic locations. Figure 3 indicates which TVOIs inside the specimens were imaged. In specimens NT6-2 and NT1-2, two radial paths were covered in the net section, spanning the complete diameter. This was done to assess if void distribution was close to axisymmetric. In the other two specimens, a radial path was followed both at the net section and outside the notched region, in order to

evaluate void growth in the notch. For NT6-1, only part of the radial path outside the notch was covered, but an additional TVOI was obtained along specimen axis, in order to extract information on the axial void distribution.

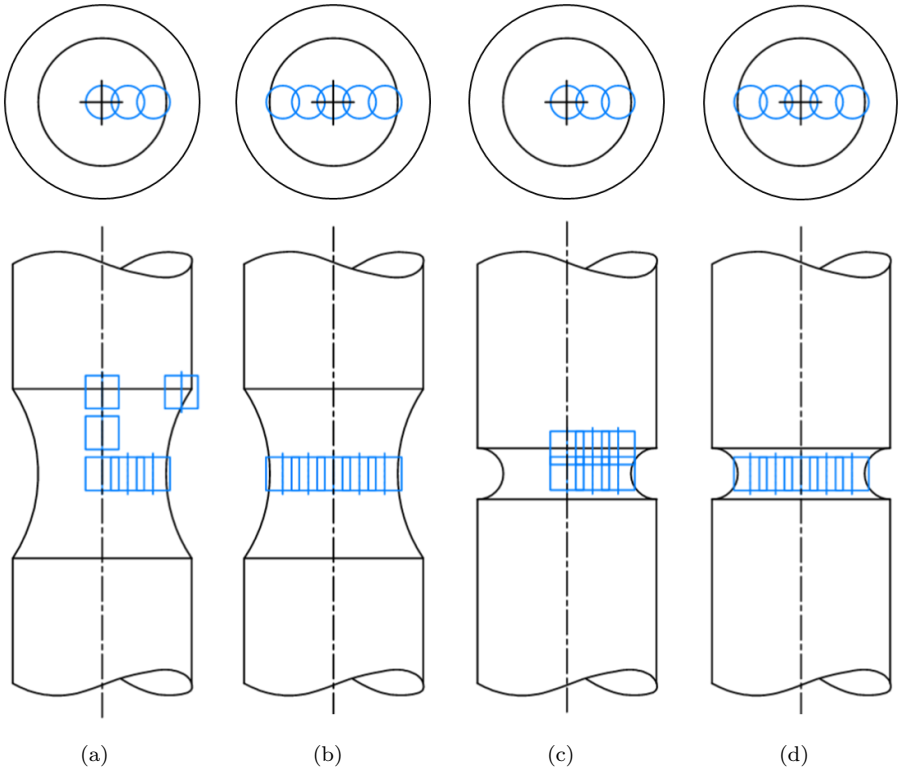

Fig. 3 SRCT: Positions of the Tomographic Volumes Of Interest (TVOI) for the scanned specimens: **a)** NT6-1, **b)** NT6-2 **c)** NT1-1, **d)** NT1-2.

An image analysis segmentation procedure was applied to the tomography volumes. Voids were recognized as local minima of the greyscale distribution [11]. The algorithm could erroneously identify voids on the surface of the specimen, therefore the edge was excluded from the analysis. After carrying out the segmentation, void position, volume and equivalent ellipsoid dimensions were calculated.

2.5 Volumes and Surfaces of Interest

To describe void volume fraction distribution inside the tomography volumes, it is necessary to define a Statistical Volume of Interest (SVOI), over which a local void volume fraction is calculated. It needs to be small enough to ensure

homogeneity of void volume fraction inside of it, but large enough to contain multiple voids. The choice of SVOI is therefore microstructure-dependent. In a similar analysis conducted on Polyamide 6, it was defined as a (50 µm × 50 µm × 40 µm) cuboid [11]. For the work presented here, it was decided to use a cubic SVOI. A study was conducted to evaluate the influence of SVOI size on the void volume fraction measurement. For small SVOI sizes, void fraction shows strong oscillations. It stabilizes when the edge length reaches 200 µm and does not change significantly, as the size of SVOI is further increased. Given these results, an edge length of 250 µm was chosen for the cubic SVOI used in the study presented here.

Each SVOI is provided with several statistics: number of voids, coordinates of individual voids, their volume and equivalent ellipsoid dimensions. To determine the void volume fraction at a given location, a SVOI with a barycentre at that point is considered. Void volume fraction is calculated as the summed volume of all voids inside the SVOI divided by the volume of the SVOI.

Figure 4 illustrates how the concept of SVOI is used to evaluate void volume fraction distribution along a radial path in the plane of the net section of a specimen. First, it is necessary to obtain three TVOIs spanning the distance from the axis to the edge of the specimen. Then, adjacent SVOIs are stacked, with their barycentres located along the radial path. The void volume fraction along the path is then measured from these SVOIs.

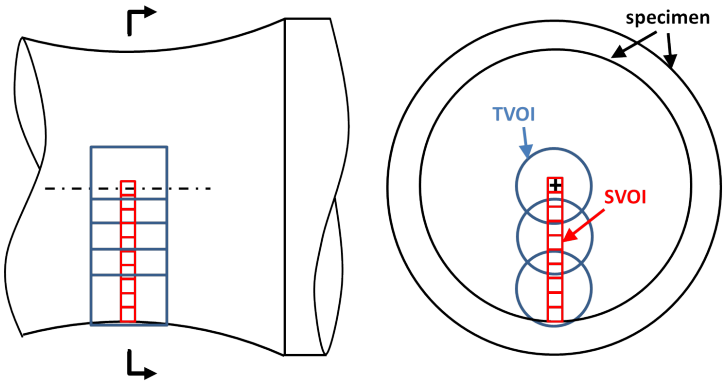

Fig. 4 SRCT: volumes of interest in the notched region of the specimen. Black line represents the edge of the specimen, each blue cylinder is a Tomographic Volume of Interest (TVOI) corresponding to a single tomography volume and each red cube is a Statistical Volume of Interest (SVOI).

By analogy to the SVOI concept, a Statistical Surface of Interest (SSOI) was introduced for the SEM results. In order to simplify the comparison with SRCT results, it was decided to use a square of (250 µm × 250 µm). Figure 5 illustrates how void area fraction is sampled along several radial paths. A sequence of adjacent SSOIs is constructed along a given path. For each SSOI, the number of voids is known. Histograms are available for the maximum Feret

diameter of the voids. Depending on the size of the scanned part of the fracture surface, several radial paths can be sampled. In this case, three radial paths are represented.

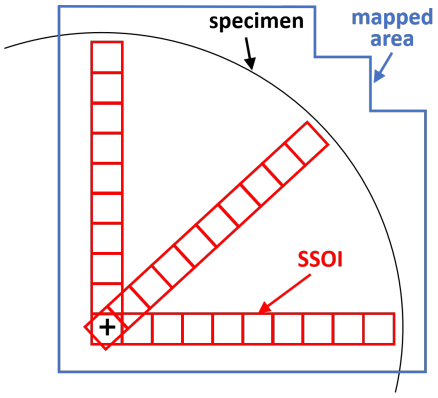

Fig. 5 SEM: illustration of the process of calculating the radial distribution of void volume fraction on the fracture surface. Statistical Surfaces of Interest (SSOI) represented in red are squares with a 250 µm edge. The mapped part of the fracture surface is outlined in blue. The edge of the specimen is marked with a black line.

2.6 Finite element modelling

Finite element analysis is required to compute the local stress tensor in the specimens. The experimental results were used to calibrate a numerical model of the material. Taking advantage of symmetry, only a half of one notch was meshed. Eight-node quadrilateral axisymmetric elements (CAX8) were used. The mesh was most refined in the notch, with element size of approximately 50 µm. A displacement boundary condition was applied at the top edge of the mesh. Its value was based on the displacement ΔL measured from the tensile tests. The simulations were stopped when ΔL reached the value at which the simulated specimens failed in the tests.

The constitutive law used was a modified Gurson-Tvergaard-Needleman (GTN) model. It consists of the original micromechanical approach of Gurson [17], extended based on phenomenological considerations by Tvergaard [18] and Needleman [9]. It is capable of taking into account time-dependent deformation, as well as volume variation caused by void growth and nucleation [19]. Void volume fraction being an internal variable of the model, its distribution can be compared to that measured experimentally. In the work presented, this modelling approach is applied to a thermosetting polymer. Only the principal equations of the constitutive law are recalled here. A more detailed description can be found elsewhere, e.g. in Laiarinandrasana et al. [4].

The GTN porous potential is governed by the following equation, implicitly defining an effective scalar stress: σ^* [20]:

$$\Phi(\boldsymbol{\sigma}, \sigma^*, f) = \frac{\sigma_{eq}^2}{\sigma^{*2}} + 2q_1 f \cosh(\frac{q_2 \mathrm{tr}(\boldsymbol{\sigma})}{2\sigma^*}) - (1 + q_1^2 f^2) = 0, \tag{1}$$

where σ_{eq} is the von Mises stress, f is the void volume fraction, while q_1 and q_2 are constant material coefficients. The yield surface is defined as:

$$\varphi = \sigma^* - R, \tag{2}$$

where R is the flow stress modelled through:

$$R = R_0 + Q(1 - \mathrm{e}^{-bp}), \tag{3}$$

with material coefficients R_0, Q and b, and p being the cumulative plastic strain. The viscoplastic strain tensor is then written as:

$$\dot{\boldsymbol{\varepsilon}}_v = (1 - f)\dot{p}\frac{\partial \varphi}{\partial \boldsymbol{\sigma}}. \tag{4}$$

The cumulative plastic strain is governed by Norton law:

$$\dot{p} = \dot{\varepsilon}_0 \left\langle \frac{\varphi}{K} \right\rangle^n, \tag{5}$$

where $\dot{\varepsilon}_0 = 1\,\mathrm{s}^{-1}$ and K and n are material coefficients. Finally, the evolution of void volume fraction is obtained from the equation:

$$\dot{f} = (1 - f)\mathrm{tr}(\dot{\boldsymbol{\varepsilon}}_v) \tag{6}$$

Altogether, the model requires determining the values of nine material coefficients: elastic coefficients E and ν, hardening parameters R_0, Q and b, void interaction parameters q_1 and q_2 and Norton parameters K and n.

3 Results and Discussion

3.1 Data at the macroscopic scale from the tensile tests

As anticipated, all specimens failed in the net section of one of the notches. In NT6 specimens, the notch which would break showed an increasingly larger NOD shortly prior to failure than the second notch. The failure of NT1 specimens was more brittle, with less discernible radial reduction and little difference between the two notches. This can be verified from Figure 6, showing NOD as a function of $\Delta L/L_0$ for the four studied specimens (NT6-1, NT6-2, NT1-1 and NT1-2). The two types of dashed lines correspond to the two notches. There are two lines for each notch, each one representing a single measurement, as explained in Section 2.2. The solid bold line is the average of all four measurements. It can be seen that while for NT6 a higher NOD

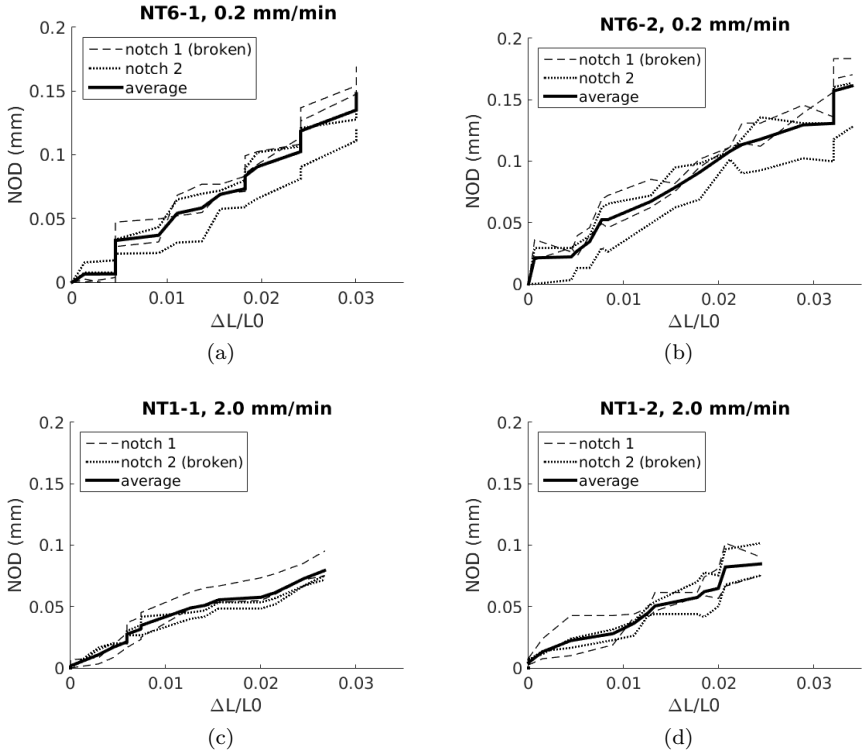

Fig. 6 Notch opening displacement (NOD) measured from photographs taken in situ. NOD was calculated from the measurements of $a^{(i)}, i = 1, 2, 3, 4$ (see Figure 2). The dashed lines correspond to the measurements on either side of one notch, and the dotted lines to those on the other one. The solid line is the average of the four measurements. For NT6, larger deformation was measured in the failing notch, but no such correlation was observed in NT1. **a)** Specimen NT6-1, **b)** Specimen NT6-2, **c)** Specimen NT1-1, **d)** Specimen NT1-2.

allows a prediction that the notch will break, there is no such correlation for NT1.

Figure 7a shows the average values of NOD with respect to $\Delta L/L_0$ for all tested specimens. The curves show a dependence on notch root radius and deformation rate. A good linear correlation between $\Delta L/L_0$ and NOD is an indication that the deformation of the specimen takes place predominantly within the notched region. It was therefore assumed that no void growth occurred outside the notch. In the analysis of the tomography data, the void volume fraction outside the notch is treated as equivalent to the initial one.

Re-necking is a phenomenon in which necking appears in the net section of an initially notched specimen. It has been described for semi-crystalline materials [4][5]. For the epoxy studied, re-necking was observed in the NT6 specimens, manifesting through a strong increase in radial reduction, shown in Figure 7b in function of the normalized displacement. In semi-crystalline polymers, this increase is followed by a plateau, which was not present in

epoxy. For the NT1 epoxy specimens, no re-necking was observed and the radial reduction curve was approximately linear.

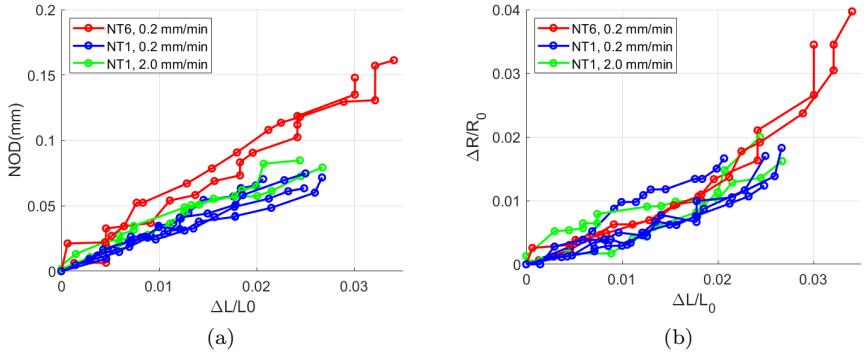

Fig. 7 Macroscopic measurements: **a)** Notch opening displacement as function of normalized measured displacement. **b)** Radial contraction as function of normalized measured displacement.

Figure 8 shows the net stress as a function of notch opening displacement. Net stress is defined as load divided by the net section area. Strain softening was observed in NT6 specimens near the end of the tests. This, together with an increased rate of radial reduction mentioned above, points to a more intensive void growth process at this stage. It is also observed that a decrease in notch root radius (and therefore an increased stress triaxiality ratio) leads to a higher maximum value of net stress, as observed previously for semi-crystalline polymers [4].

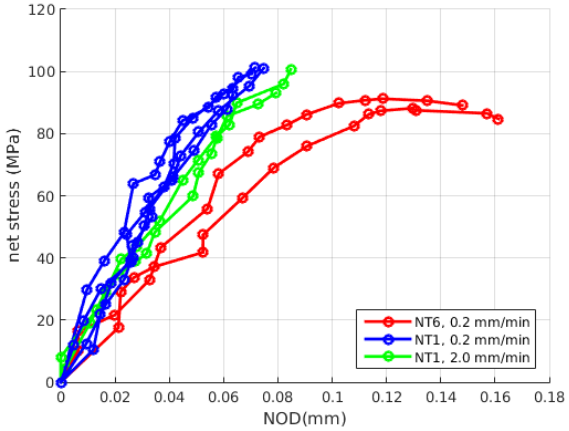

Fig. 8 Load as function of notch opening for NT6 and NT1 specimens.

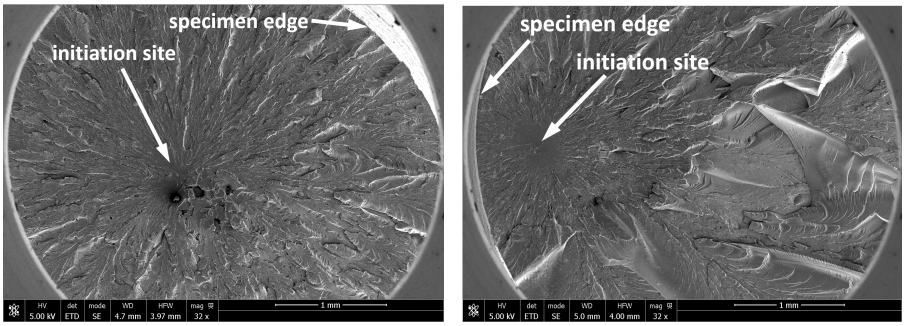

(a) (b)

Fig. 9 SEM: general view of the fracture surfaces showing the different site of initiation depending on the geometry. **a)** Specimen NT6-2, **b)** Specimen NT1-1.

An unexpected strain rate effect was observed for NT1 specimens, where a higher loading speed led to a slight stiffness reduction. This could be an effect of the significant deformation gradient in the net section of the specimens. The maximum net stress value was not affected significantly by loading speed. It is assumed that strain rate does not influence damage development and therefore void volume fraction can be treated as equivalent between NT1 specimens loaded at different speeds.

3.2 Data at the microscopic scale

3.2.1 SEM

Failure initiation Figure 9 shows the general view of representative fracture surfaces for the NT1 and NT6 geometries. For all specimens, the initiation zone was surrounded by "rivers" (striations), forming a fan-like pattern propagating through the whole fracture surface. No extended fibrils were observed, pointing to a predominantly brittle failure. Numerous dimples could be seen on the fracture surfaces, with dimensions in the order of several microns. These corresponded to voids cut in half due to specimen failure, as confirmed by their symmetric presence on both sides of the fracture surfaces.

A closer observation of the failure initiation sites revealed several types of critical defects. In a single case (Specimen NT1-2), the failure initiated at an unidentified quasi-spherical inclusion, shown in Figure 10a. Most commonly, failure initiated at a cluster of voids, such as shown in Figure 10b. In many cases, the voids showed signs of coalescence and their dimensions were on average larger than those measured in tomography observations. This points to significant void growth shortly before failure. Another observed type of a critical defect was a cluster of voids with embedded particles (Figure 10c). Energy-dispersive X-ray spectroscopy showed that the spectrum of the particles was very close to that of epoxy, suggesting that they were a result

of incomplete polymerization. Generally, critical defects can be described as having an oblate shape, with a diameter of approximately 50 µm and a 5 µm height.

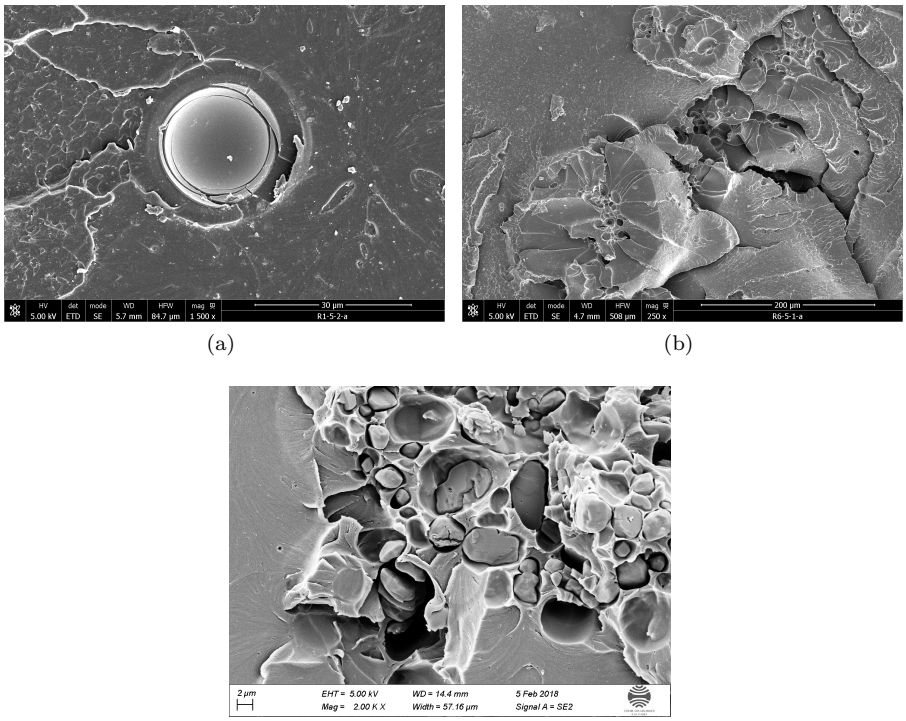

(a) (b)

(c)

Fig. 10 SEM images of fracture initiation sites: **a)** unidentified inclusion (Specimen NT1-2), **b)** void cluster (Specimen NT6-1), **c)** cluster of voids with particles inside (Specimen NT1-3).

Figure 11 shows the location of failure initiation sites for all tested specimens. For NT6 specimens, the initiation sites were consistently located near the specimen axis. In turn, the failure of all NT1 specimens initiated significantly off-axis, at approximately 80 % of the maximum net section radius. This shows that notch root radius strongly influences damage development in the specimens. A similar influence of notch geometry was previously observed for semi-crystalline polymers [10].

Void area fraction The stitched SEM images were used to characterize the radial void distribution on the fracture surfaces. Several hundred voids were identified on each mapped specimen and classified as detailed in Section 2.3. The measured Feret diameter of the voids was typically between 1 µm and 20 µm.

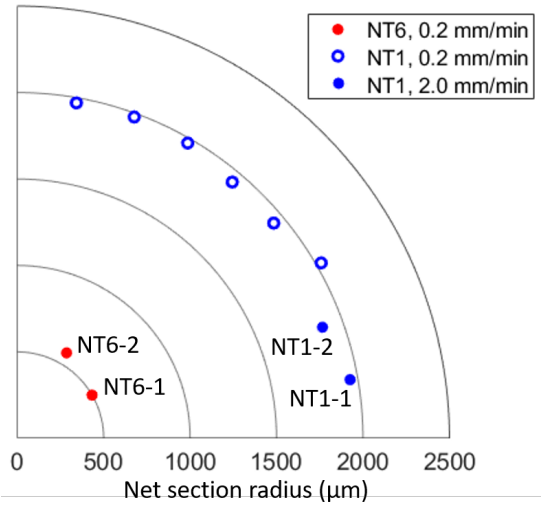

Fig. 11 Radial positions of the failure initiation loci. Each data point corresponds to one specimen. Indicated with their references are the specimens for which SEM and SRCT results are presented.

Figure 12 shows the void area fraction with respect to the normalized radius in NT6 specimens, measured along three radial paths. The radius was normalized by the radius of the gauge section ($R_{max} = 3.5\,\text{mm}$). This was done to account for the fact that voids formed during the curing process, before the notches were machined. The void fractions calculated in the SVOIs are marked with open circles and those on the same radial path are connected by a dashed line. The thicker solid curve is a manually fitted trend line, highlighting the observed tendencies, together with the associated large scatter band. For both specimens, void fraction reached its maximum near the axis of the specimen, in the vicinity of the failure initiation sites.

For the NT1 specimens, void distribution shown in Figure 13 was distinctly different than for NT6. Highest void fraction was mostly present near the edge of the specimen, at around 80 % of the net section radius, or approximately $0.6R_{max}$. Analogously to the NT6 geometry, the highest void fraction was located close to the failure initiation site. This provides proof of fast void growth in the last stage before specimen failure.

3.2.2 SRCT

Similarly to SEM observations, SRCT revealed a presence of numerous microscale level voids inside the epoxy specimens. On average, almost 12 000 voids were identified inside a single TVOI. Observed void dimensions were mostly in the order of 1 µm to 10 µm and their shapes were predominantly close to spherical. Clusters of voids were commonly observed.

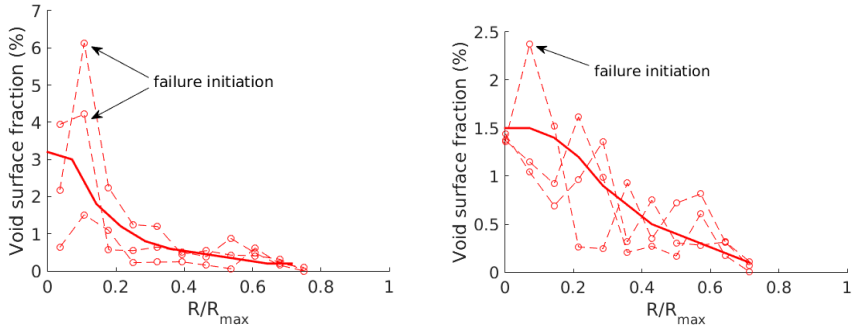

Fig. 12 SEM: radial void fraction distribution in the net section measured after failure. **a)** Specimen NT6-1, **b)** Specimen NT6-2. N.B. the y-axis range is different in the two plots to simplify the comparison of void growth tendencies between the specimens.

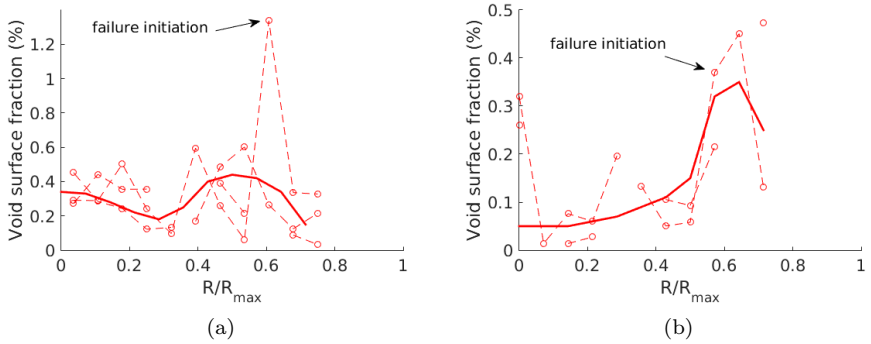

Fig. 13 SEM: radial void fraction distribution. **a)** Specimen NT1-1, **b)** Specimen NT1-2. N.B. the y-axis range is different in the two plots to simplify the comparison of void growth tendencies between the specimens.

The SRCT data paired with SEM results allow plotting the radial distribution of void volume fraction at three consecutive stages:

1. *initial state*, corresponding to the SRCT results outside the notch, as discussed in Section 3.1
2. *in the net section shortly before failure* - SRCT at the notch
3. *after failure*, obtained through SEM fractography

Figure 14 compares the evolution of void volume fraction (in blue) and void number (in red) for a specific, but representative, case of NT6-1. A shift can be observed from the dashed blue line (stage 1) to the solid blue line (stage 2). This shift does not appear for the red lines. It can be concluded that there is no void nucleation between the two recorded states and the increase in void volume fraction is uniquely due to the growth of pre-existing voids.

For specimens NT6-2 and NT1-2, no tomography data were gathered outside the notch due to limited synchrotron beam time and so only the stages

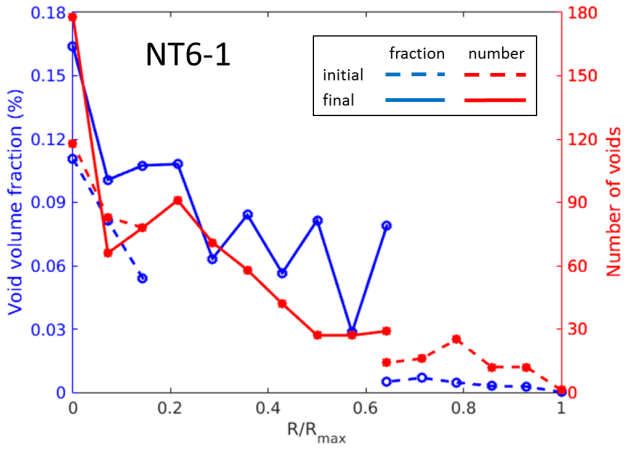

Fig. 14 SRCT: comparison of void volume fraction vs void number in the initial stage and in the notch. The number of voids does not differ significantly between the two states, while the void volume fraction is clearly higher in the notch, indicating void growth.

2 and 3 of the void evolution are available. Figures 15 and 16 show the evolution of radial void fraction through these three stages in the four studied specimens. Open square markers indicate initial void fraction values measured from the SRCT volumes. Open circles correspond to the SRCT measurements in the net section. Fitting lines are added for both the initial (dashed blue line) and the intermediate state (solid blue). For SEM, discussed in more detail in the previous section, the individual experimental points are omitted this time and only the fitting line is shown. The coordinates of the failure initiation sites are marked with arrows. Void fractions measured via SEM are much higher than those from SRCT. This can be explained by several factors, such as void growth in the broken notch shortly before failure and the closing of voids in the unbroken notches after unloading. Finally, the elliptical form of many voids observed in fractography together with the area measurement based on the maximum Feret diameter can lead to an overestimation of a void's cross-sectional area. To make the comparison between SEM and SRCT easier, the SEM results are shown on a separate scale (right hand y-axis). Below, an interpretation of the results is presented for each specimen.

Specimen NT6-1 (Figure 15a) One radial path was considered both at the net section and outside the notch. No TVOIs were obtained outside the notch for $0.2 \leq R/R_{max} \leq 0.6$. At both stages, a clear gradient of void volume fraction is present, with highest values observed near the axis of the specimen. This gradient is principally due to a higher number of voids inside some SVOIs and not their larger dimensions. At the notch, the void fraction is consistently higher at all radial coordinates in comparison with the initial state. This increase is due the larger void volumes at the notch, while the difference in the number of voids per SVOI is minor.This indicates that the main responsible

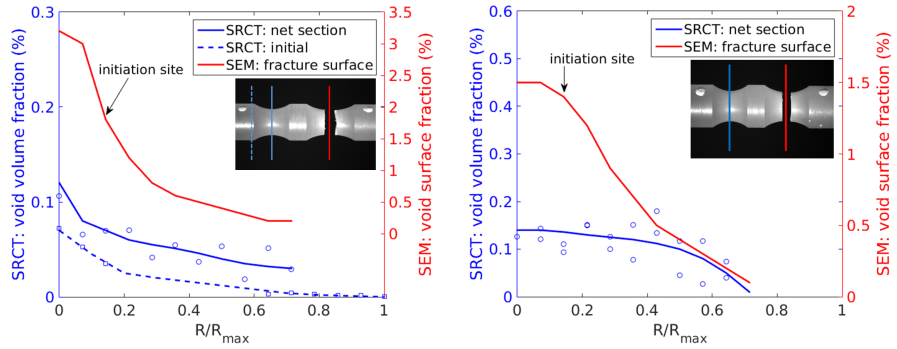

Fig. 15 NT6 radial void volume fraction evolution. **a)** Specimen NT6-1, **b)** Specimen NT6-2. N.B. the y-axis range is different in the two plots to simplify the comparison of void growth tendencies between the specimens.

mechanism is void growth and not nucleation. SEM fractography results show a similar curve to SRCT, with highest void fraction near the specimen axis, in particular around the failure initiation site.

Specimen NT6-2 (Figure 15b) As mentioned previously, only stages 2 and 3 of void evolution are available for this specimen. At the notch, two radial lines were mapped using SRCT data, spanning the whole diameter of the specimen. The radial void fraction gradient is visible in this specimen too, although with a plateau near specimen axis, not observed for NT6-1. This is explained by a more uniform distribution of the voids inside the SVOIs. SEM fractography shows a similar void fraction evolution as in NT6-1: maximum void area fraction is observed near the axis of the specimen, as was also observed in semi-crystalline polymers [10].

Specimen NT1-1 (Figure 16a) Initial void distribution is not uniform. Void fraction is highest near the specimen axis, with a similar gradient to that of Specimen NT6-1. SRCT results in the net section show two areas with significant difference from the initial state. Firstly, the void fraction near the specimen axis is higher. The number of voids is also significantly higher there, so this difference is regarded as being caused by the initial porosity scatter. A second area of increased void volume fraction is located close to the net section edge ($0.4 \leq R/R_{max} \leq 0.7$). In that case, the increased porosity results from a higher average void volume, indicating void growth. Void fraction measured from the SEM images is higher than that from SRCT, although the difference between the two is lower than in the NT6 specimens. This indicates a lower intensity of the void growth process, which is consistent with the lower measured radial reduction, as discussed in Section 3.1. As mentioned in Section 3.2.1, fracture surface observations revealed the highest void fraction at approximately $0.6R_{max}$. This shows that the smaller notch root radius causes

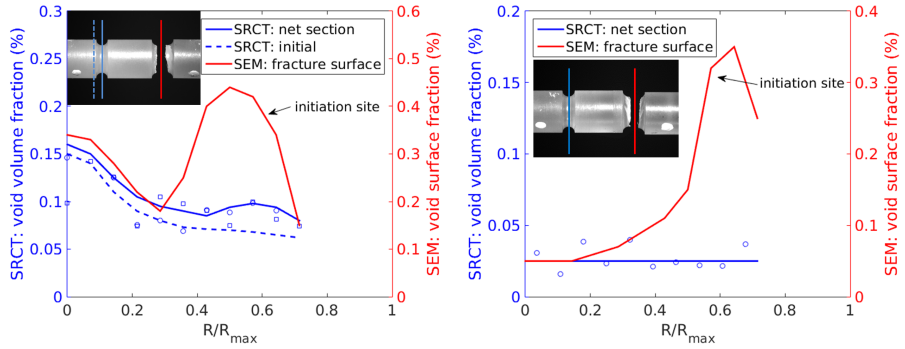

Fig. 16 NT1 radial void volume fraction evolution. **a)** Specimen NT1-1, **b)** Specimen NT1-2. N.B. the y-axis range is different in the two plots to simplify the comparison of void growth tendencies between the specimens.

the void growth to occur predominantly away from the axis of the specimen, as also observed for semi-crystalline polymers [10].

Specimen NT1-2 (Figure 16b) No initial void fraction data were collected for this specimen. Both for the net section SRCT and SEM fractography results, the void fraction values are the lowest recorded for all specimens. Compared to the other specimens, the SRCT scans show fewer voids. The homogeneous void distribution at the net section is probably due to a uniform initial distribution in that region. The passage from notch SRCT to SEM shows that most void growth takes place at a similar location as for the Specimen NT1-1 discussed above ($0.4 \leq R/R_{max} \leq 0.7$). In this case, failure initiated at an unidentified inclusion, as discussed in Section 3.2.1.

3.3 Finite element modelling

Inverse optimization All finite element calculations were performed using an in-house finite element code Z-Set [21]. A built-in routine was used to calibrate the model coefficients using the inverse optimization method. Initial void volume fraction was set to be homogeneous at 0.05 %, in the order of magnitude observed experimentally as seen in Figures 15 and 16. The values of E and ν were determined experimentally at 3400 MPa and 0.42, respectively. The values of $q_1 = 1.0$ and $n = 2.0$ were fixed arbitrarily in advance. The optimization process took into account both macroscopic and microscopic data. At the macroscopic scale, optimization on load with respect to NOD (not the cross-head displacement) gave several sets of possible coefficients. The experimental points were sampled from two NT6 and from four NT1 specimens. When comparing the location of the maximum void volume fraction locally, the best corresponding set of material parameters was selected. It should be pointed

out that in this procedure, the initial void volume fraction was considered to be homogeneous. Therefore, specimens with an approximately uniform initial void volume fraction were used for the comparison, i.e. NT6-2 and NT1-2. The optimized values of the GTN coefficients are presented in Table 1.

Table 1 Optimized coefficients of the GTN model.

E	ν	R_0	Q	b	q_1	q_2	K	n
3400 MPa	0.42	15 MPa	58 MPa	500	1.0	1.6	440 MPa	2.0

The calibrated numerical model shows a good match for both the macroscopic and microscopic curves. The comparison of numerical and experimental curves of net stress vs NOD is presented in Figure 17. The simulation captures successfully the higher stiffness of NT1, as well as the stress softening in NT6. The simulated radial void volume fraction in the net section for an initially uniform distribution of 0.05 % is plotted in Figure 18. Void volume fraction evolution shows a good qualitative agreement with the experiments, with most growth at the specimen axis for NT6 and near the net section edge for NT1.

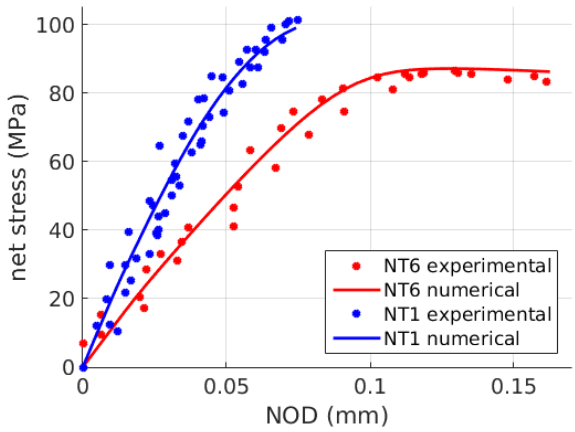

Fig. 17 FEM: Load as a function of notch opening displacement for NT1 and NT6 geometries. Displacement speed: 0.2 mm/min. Comparison with experimental results.

Non-uniform initial void volume fraction The initial void volume fraction observed experimentally in specimens NT6-1 and NT1-1 was not uniform. Therefore, a simulation was carried out with a linear radial gradient of void fraction changing from 0.10 % at the axis of the specimen to 0.05 % at the edge of the net section. For this case, the simulated void volume fraction in the net

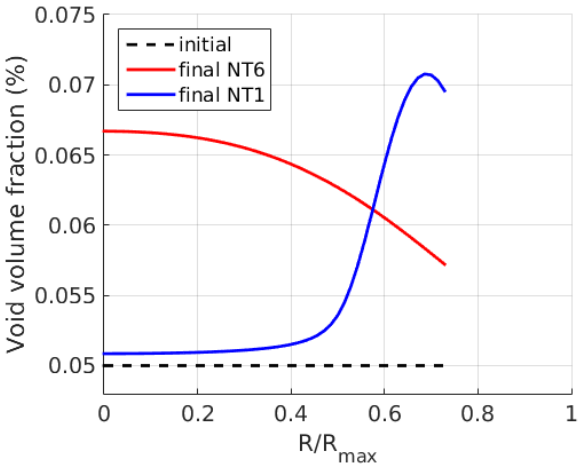

Fig. 18 FEM: void volume fraction in the net section of an NT1 and an NT6 specimen at failure. Uniform initial void fraction of 0.05 %.

section at failure is shown in Figure 19. Fastest void growth takes place in the same regions as for the uniform initial porosity case. However, the maximum value of void volume fraction is significantly higher for NT6, since the area of maximum void growth is also that of the maximum initial void fraction. This agrees with the experimental results, where NT6 specimens showed higher void fractions overall than NT1. The results show a good agreement with the experimental void distribution plotted in Figures 15a and 16a. It is worth noting that for NT1-1, void volume fraction experiences the fastest growth near the notch root radius, while the maximum void volume fraction is located close to the specimen axis. This effect is captured numerically.

Stress distribution The GTN model based on the mechanics of porous media allows computing the stress tensor at the local scale, homogenizing the epoxy and the voids into a single continuum. Figures 20 and 21 show the computed contour maps of hydrostatic pressure and the maximum principal stress in the NT6 and NT1 specimens, respectively, obtained for a uniform initial void volume fraction of 0.05%. For a given specimen geometry, the location of the maximum hydrostatic pressure is the same as that of the maximum principal stress. However, there are differences between the two geometries. For NT6, the maximum values of stress are present at the centre of the specimen. For NT1, the maximum is located in the proximity of the net section edge. The maximum principal stress is always greater than hydrostatic pressure, which agrees with the fact that the maximum principal stress is roughly equal to the sum of hydrostatic pressure and the shear stress represented through the equivalent von Mises stress [22]. It should be noted that the hydrostatic pressure is the stress related to the volumetric strain which is affected by void growth.

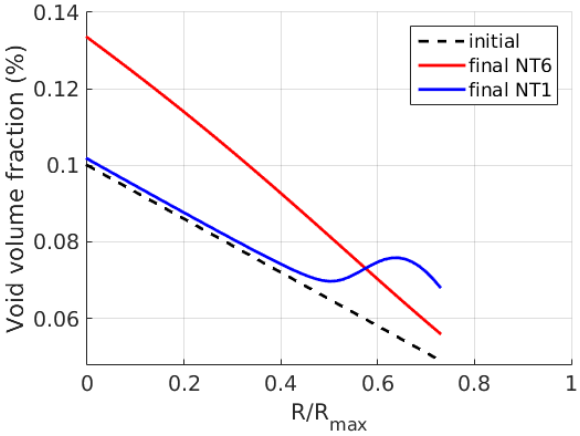

Fig. 19 FEM: void fraction evolution in the net section of an NT1 and an NT6 specimen, given an initial porosity gradient. $R_{max} = 3.5\,\text{mm}$.

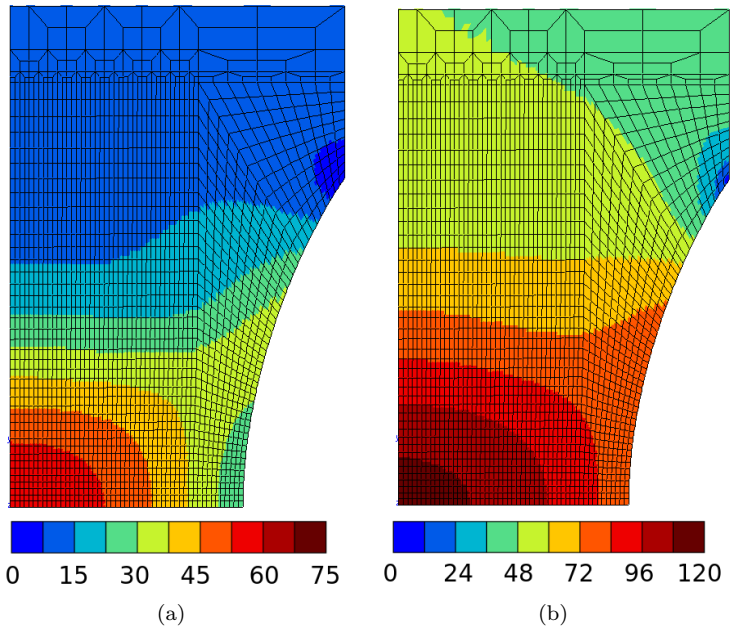

Fig. 20 FEM: stress contour map (MPa) at failure in the NT6 specimen. a) hydrostatic pressure, b) maximum principal stress.

Failure criterion As mentioned earlier, radial void distribution in the net section of specimen NT1-1 is of particular interest. While the fastest void growth takes place close to the edge of the specimen, maximum void volume fraction at failure is recorded at the axis of the specimen. This highlights that unlike for semi-crystalline polymers, a critical value of void fraction cannot be used

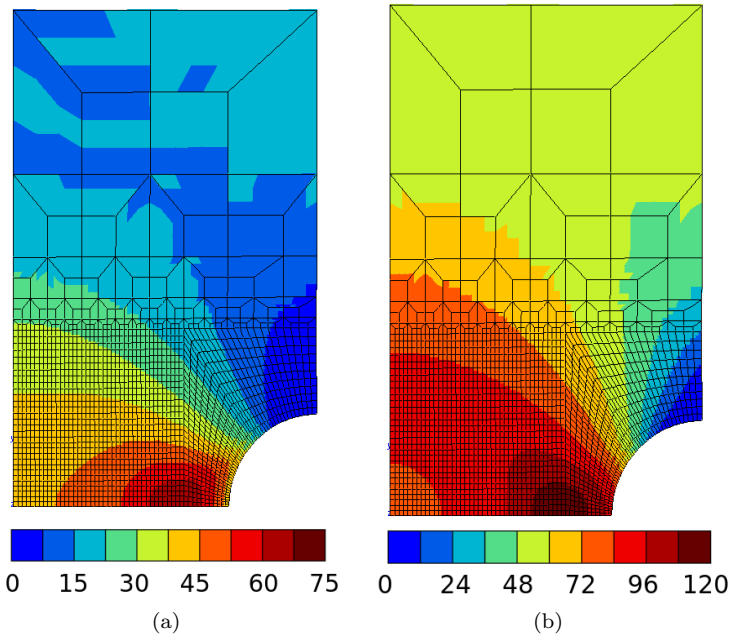

Fig. 21 FEM: stress contour map (MPa) at failure in the NT1 specimen. a) hydrostatic pressure, b) maximum principal stress.

as a failure criterion. For brittle materials, such as the epoxy studied, a more appropriate criterion would be based on the existence of a critical defect in a region where the stress is greater than or equal to a critical value. The failure criterion can be further investigated by looking at the radial distribution of the maximum principal stress in the net section shown in Figure 22, together with the locations of the critical defects as shown in Figure 11. It can be seen that the initial void distribution has a minor influence on the predicted stress magnitude and distribution. The shaded regions in the figure indicate the range of radial coordinates of the critical defects that triggered the brittle failure. It can then be concluded that the critical maximum principal stress is approximately 110 MPa.

4 Conclusions

The study presented in this article aimed at quantifying void growth inside a thermosetting epoxy resin and improving the understanding of the damage processes taking place. To this end, double-notched round bars with two different notch root radii were manufactured and tested in tension. Afterwards, the fracture surfaces were observed via SEM, while the unbroken notches were scanned using SRCT. The combination of both techniques allowed the assessment of void growth at different stages of damage. Void position and size were

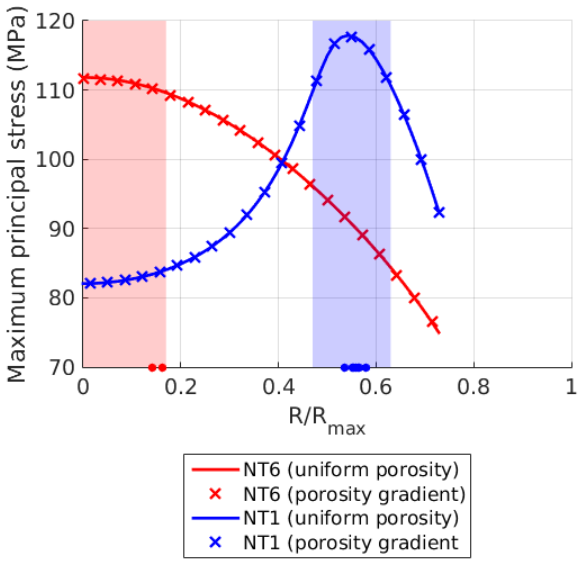

Fig. 22 FEM: main principal stress in the net section at failure. The dot markers correspond to experimentally observed failure initiation sites for NT6 (red) and NT1 (blue). The shaded areas indicate regions where a critical defect can coincide with a critical stress for the respective geometries, leading to failure.

measured and a Statistical Volume of Interest (SVOI) was defined to evaluate void volume fraction distribution. An initially non-uniform void distribution was observed in most cases. The comparison of consecutive stages of damage development allowed areas exhibiting most void growth to be identified. For NT6 specimens, those were near the specimen axis, whereas for NT1 they were located at approximately 80 % of the maximum net section radius. The failure originated at a critical defect: a cluster of voids, a cluster of particles and in one case at an unidentified inclusion. The dependence of failure initiation location on notch root radius highlights the sensitivity of the material to multiaxial stress states.

The experimental observations at the macro- and the microscale were used to calibrate a numerical model of the epoxy, using a Gurson-Tvergaard-Needleman (GTN) constitutive law. The simulations predicted the highest values of the maximum principal stress in the areas where failure initiation was observed experimentally. The GTN model was shown to be an appropriate choice for modelling an amorphous polymer, being able to handle low initial void fractions ($\approx 0.1\%$) and non-uniform void distributions. A critical void fraction was determined not to be a suitable failure criterion for a thermosetting polymer. A different criterion was proposed, based on a combination of

a critical value of the maximum principal stress and the presence of a critical defect.

The results presented highlight the significance of multiaxial stresses in the failure of polymeric materials. The finite element model can be applied to model epoxy matrices, commonly used in high-performance fibre-reinforced composites. This would improve the understanding of the mechanical response of this materials at the microscale, where the polymer can be subjected to a highly multiaxial stress state. Furthermore, by quantifying the probability of a critical defect presence in the material, a stochastic model can be built, accounting for the scatter of failure initiation sites and net stress in the notched specimens.

Conflict of interest

The authors declare that they have no conflict of interest.

Acknowledgements The research leading to these results has been carried out within the framework of the FiBreMoD project and has received funding from the European Union's Horizon 2020 research and innovation programme under Marie Skodowska-Curie grant agreement No 722626. The authors would also like to acknowledge Synchrotron SOLEIL for providing the synchrotron radiation facilities (Proposal 20180023) and thank Jonathan Perrin, Mario Scheel and Timm Weitkamp for their assistance in using the beamline ANATOMIX. ANATOMIX is an Equipment of Excellence (EQUIPEX) funded by the "Investments for the Future" programme of the French National Research Agency (ANR), project "NanoimagesX", grant No ANR-11-EQPX-0031. Christian Breite gratefully acknowledges Stepan V. Lomov and Larissa Gorbatikh from KU Leuven for their fruitful discussions and supervision of his PhD. Yentl Swolfs acknowledges FWO Flanders for his postdoctoral fellowship.

References

1. Laiarinandrasana, L., Morgeneyer, T.F., Cheng, Y., Helfen, L., Le Saux, V., Marco, Y.: Microstructural observations supporting thermography measurements for short glass fibre thermoplastic composites under fatigue loading. Contin. Mech. Thermodyn. pp. 1–19 (2019)
2. Scott, A.E., Sinclair, I., Spearing, S.M., Thionnet, A., Bunsell, A.R.: Damage accumulation in a carbon/epoxy composite: Comparison between a multiscale model and computed tomography experimental results. Compos. Part A Appl. Sci. Manuf. **43**(9), 1514–1522 (2012)
3. Swolfs, Y., Verpoest, I., Gorbatikh, L.: A review of input data and modelling assumptions in longitudinal strength models for unidirectional fibre-reinforced composites. Compos. Struct. **150**, 153–172 (2016)
4. Laiarinandrasana, L., Besson, J., Lafarge, M., Hochstetter, G.: Temperature dependent mechanical behaviour of PVDF: Experiments and numerical modelling. Int. J. Plasticity **25**(7), 1301–1324 (2009)
5. Challier, M., Besson, J., Laiarinandrasana, L., Piques, R.: Damage and fracture of polyvinylidene fluoride (PVDF) at 20 degree C: Experiments and modelling. Eng. Fract. Mech. **73**, 79–90 (2006)
6. Boisot, G., Laiarinandrasana, L., Besson, J., Fond, C., Hochstetter, G.: Experimental investigations and modeling of volume change induced by void growth in polyamide 11. Int. J. Solids Struct. **48**(19), 2642–2654 (2011)

7. Selles, N., King, A., Proudhon, H., Saintier, N., Laiarinandrasana, L.: Time dependent voiding mechanisms in polyamide 6 submitted to high stress triaxiality: experimental characterisation and finite element modelling. Mech. Time-Depend. Mat. **22**(3), 351–371 (2018)
8. Morelle, X.P., Chevalier, J., Bailly, C., Pardoen, T., Lani, F.: Mechanical characterization and modeling of the deformation and failure of the highly crosslinked RTM6 epoxy resin. Mech. Time-Depend. Mat. **21**(3), 419–454 (2017)
9. Tvergaard, V., Needleman, A.: Analysis of the cup-cone fracture in a round tensile bar. Acta Metall. **32**(1), 157–169 (1984)
10. Cayzac, H.A., Sa, K., Laiarinandrasana, L.: Damage based constitutive relationships in semi-crystalline polymer by using multi-mechanisms model. Int. J. Plasticity **51**, 47–64 (2013)
11. Laiarinandrasana, L., Klinkova, O., Nguyen, F., Proudhon, H., Morgeneyer, T.F., Ludwig, W.: Three dimensional quantification of anisotropic void evolution in deformed semi-crystalline polyamide 6. Int. J. Plasticity **83**, 19–36 (2016)
12. Cantwell, W.J., Roulin-Moloney, A.C., Kaiser, T.: Fractography of unfilled and particulate-filled epoxy resins. J. Mater. Sci. **23**(5), 1615–1631 (1988)
13. Schindelin, J., Arganda-Carreras, I., Frise, E., Kaynig, V., Longair, M., Pietzsch, T., Preibisch, S., Rueden, C., Saalfeld, S., Schmid, B., Tinevez, J.Y., White, D.J., Hartenstein, V., Eliceiri, K., Tomancak, P., Cardona, A.: Fiji: an open-source platform for biological-image analysis. Nat. Methods **9**, 676–682 (2012)
14. Preibisch, S., Saalfeld, S., Tomancak, P.: Globally optimal stitching of tiled 3D microscopic image acquisitions. Bioinformatics **25**(11), 1463–1465 (2009)
15. Feret, L.: La grosseur des grains des matières pulvérulentes. Premières Communications de la Nouvelle Association Internationale pour l'Essai des Matériaux, groupe D pp. 428–436 (1930)
16. Weitkamp, T., Scheel, M., Giorgetta, J.L., Joyet, V., Le Roux, V., Cauchon, G., Moreno, T., Polack, F., Thompson, A., Samama, J.P.: The tomography beamline ANATOMIX at Synchrotron SOLEIL. J. Phys. Conf. Ser. **849**, 12–37 (2017)
17. Gurson, A.L.: Continuum theory of ductile rupture by void nucleation and growth: Part I - Yield criteria and flow rules for porous ductile media. J. Eng. Mater. Technol. **99**(1), 2–15 (1977)
18. Tvergaard, V.: Influence of void nucleation on ductile shear fracture at a free surface. J. Mech. Phys. Solids **30**(6), 399–425 (1982)
19. Vaz Jr., M., Andrade Pires, F.M.: A note on the thermal effects upon a Gurson-type material model. Contin. Mech. Thermodyn. **28**(3), 785–798 (2016)
20. Besson, J., Steglich, D., Brocks, W.: Modeling of crack growth in round bars and plane strain specimens. Int. J. Solids Struct. **38**(46), 8259–8284 (2001)
21. Besson, J., Foerch, R.: Large scale object-oriented finite element code design. Comput. Methods. Appl. Mech. Eng. **142**(1), 165–187 (1997)
22. Bridgman, P.W.: The stress distribution at the neck of a tension specimen. Transactions ASM **32**, 553–574 (1944)